

# Long-term survival of surface water ice on comet 67P

N. Oklay,<sup>1★</sup> S. Mottola,<sup>1</sup> J.-B. Vincent,<sup>1</sup> M. Pajola,<sup>2</sup> S. Fornasier,<sup>3</sup> S. F. Hviid,<sup>1</sup>  
D. Kappel,<sup>1</sup> E. Kührt,<sup>1</sup> H. U. Keller,<sup>4</sup> M. A. Barucci,<sup>3</sup> C. Feller,<sup>3</sup> F. Preusker,<sup>1</sup>  
F. Scholten,<sup>1</sup> I. Hall,<sup>5</sup> H. Sierks,<sup>5</sup> C. Barbieri,<sup>6</sup> P. L. Lamy,<sup>7</sup> R. Rodrigo,<sup>8,9</sup>  
D. Koschny,<sup>10</sup> H. Rickman,<sup>11,12</sup> M. F. A’Hearn,<sup>13</sup> J.-L. Bertaux,<sup>14</sup> I. Bertini,<sup>15</sup>  
D. Bodewits,<sup>13</sup> G. Cremonese,<sup>16</sup> V. Da Deppo,<sup>17</sup> B. J. R. Davidsson,<sup>18</sup> S. Debei,<sup>19</sup>  
M. De Cecco,<sup>20</sup> J. Deller,<sup>5</sup> J. D. P. Deshapriya,<sup>3</sup> M. Fulle,<sup>21</sup> A. Gicquel,<sup>18</sup>  
O. Groussin,<sup>22</sup> P. J. Gutiérrez,<sup>23</sup> C. Güttler,<sup>5</sup> P. H. Hasselmann,<sup>3</sup> M. Hofmann,<sup>5</sup>  
W.-H. Ip,<sup>24</sup> L. Jorda,<sup>22</sup> J. Knollenberg,<sup>1</sup> G. Kovacs,<sup>5</sup> J.-R. Kramm,<sup>5</sup> M. Küppers,<sup>25</sup>  
L. M. Lara,<sup>23</sup> M. Lazzarin,<sup>6</sup> Z.-Y. Lin,<sup>24</sup> J. J. Lopez Moreno,<sup>23</sup> A. Lucchetti,<sup>16</sup>  
F. Marzari,<sup>6</sup> N. Masoumzadeh,<sup>5</sup> G. Naletto,<sup>15,17,26</sup> A. Pommerol,<sup>27</sup> X. Shi,<sup>5</sup>  
N. Thomas<sup>27</sup> and C. Tubiana<sup>5</sup>

*Affiliations are listed at the end of the paper*

Accepted 2017 August 31. Received 2017 August 13; in original form 2017 April 4

## ABSTRACT

Numerous water-ice-rich deposits surviving more than several months on comet 67P/Churyumov-Gerasimenko were observed during the *Rosetta* mission. We announce the first-time detection of water-ice features surviving up to 2 yr since their first observation via OSIRIS (Optical, Spectroscopic, and Infrared Remote Imaging System) NAC (narrow angle camera). Their existence on the nucleus of comet 67P at the arrival of the *Rosetta* spacecraft suggests that they were exposed to the surface during the comet’s previous orbit. We investigated the temporal variation of large water-ice patches to understand the long-term sustainability of water ice on cometary nuclei on time-scales of months and years. Large clusters are stable over typical periods of 0.5 yr and reduce their size significantly around the comet’s perihelion passage, while small exposures disappear. We characterized the temporal variation of their multispectral signatures. In large clusters, dust jets were detected, whereas in large isolated ones no associated activity was detected. Our thermal analysis shows that the long-term sustainability of water-ice-rich features can be explained by the scarce energy input available at their locations over the first half year. However, the situation reverses for the period lasting several months around perihelion passage. Our two end-member mixing analysis estimates a pure water-ice equivalent thickness up to 15 cm within one isolated patch, and up to 2 m for the one still observable through the end of the mission. Our spectral modelling estimates up to 48 per cent water-ice content for one of the large isolated feature, and up to 25 per cent water ice on the large boulders located within clusters.

**Key words:** methods: data analysis – techniques: image processing – techniques: imaging spectroscopy – comets: individual: 67P/Churyumov-Gerasimenko.

## 1 INTRODUCTION

More than a hundred water-ice-rich exposures were putatively detected on the Northern hemisphere of comet 67P before 2015

(Pommerol et al. 2015). They are located on various types of terrains: smooth, rough, below overhangs, near cliffs either as isolated features (IFs) or in clusters (Pommerol et al. 2015). The clusters enriched in water ice have similar multispectral properties to the water-ice deposits observed on comet 9P/Tempel 1, while the large isolated ones resemble the largest water-ice deposit observed on comet 103P/Hartley 2 (Oklay et al. 2016a). The size of water-ice

\* E-mail: [Nilda.OklayVincent@dlr.de](mailto:Nilda.OklayVincent@dlr.de)

exposures observed on comet 67P are limited by the spatial resolutions achieved by the Optical, Spectroscopic, and Infrared Remote Imaging System (OSIRIS; Keller et al. 2007) narrow angle camera (NAC) during the *Rosetta* mission and vary from centimetres up to several tens of metres (see Oklay et al. 2016a, for details). There was activity i.e. jets and outbursts related to some of the observed water-ice features (Knollenberg et al. 2016; Oklay et al. 2016b; Vincent et al. 2016b).

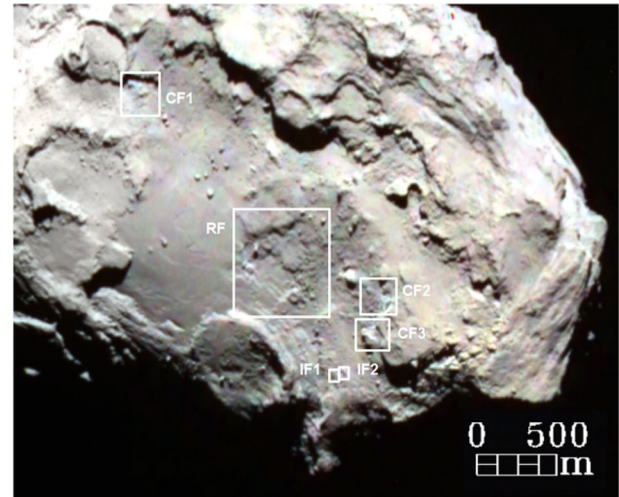
The large clusters containing individual water-ice-rich exposures seem to be formed via cliff collapse, while the large IFs seem to be formed via surface deflation. There are numerous small isolated water-ice-rich features, which are possibly exposures from beneath the surface. The deflation reported by Groussin et al. (2015) exposed a large water-ice-rich layer in the Imhotep region (see El-Maarry et al. 2015, 2016, for region definitions). Similarly, a collapse of the Aswan cliff revealed a layer enriched in water ice (Pajola et al. 2017). The water-ice-rich boulders within clusters seem to be formed during the associated cliff collapse event (see Oklay et al. 2016a, for discussions).

Long-term high-spatial resolution multispectral observations of comet 67P via OSIRIS NAC onboard ESA's *Rosetta* spacecraft allowed us to study for the first time the temporal evolution of water-ice-rich features on a comet surface for more than a year. Using OSIRIS NAC multispectral observations, water-ice-rich features located in various terrains with various lifetimes had already been detected during the *Rosetta* mission:

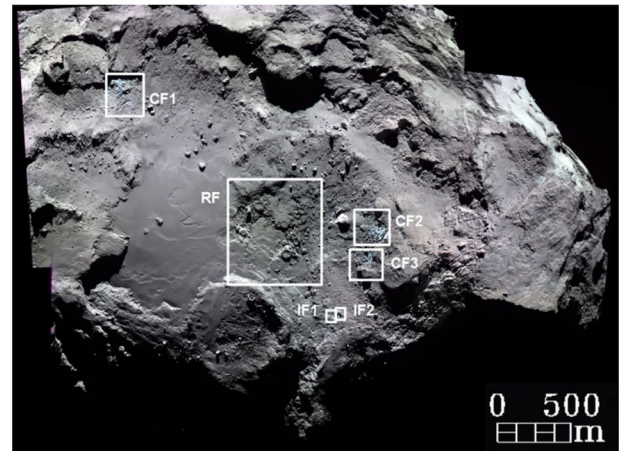
- (i) Water frost observed on local morning having lifetimes of minutes (Fornasier et al. 2016).
- (ii) Water-ice-rich features located in smooth terrains having lifetimes of about 10 d (Fornasier et al. 2016).
- (iii) Small-scale water-ice-rich features having lifetimes of days and weeks (Barucci et al. 2016; Deshapriya et al. 2016; Pommerol et al. 2015).
- (iv) Exposure of potential H<sub>2</sub>O and/or CO<sub>2</sub> ice observed on the large roundish features (RFs) formed, expanded and disappeared in Imhotep region within a month in 2015 (Groussin et al. 2015).
- (v) Water-ice-rich features located in rough terrains having lifetimes of about several months (Barucci et al. 2016; Deshapriya et al. 2016; Oklay et al. 2016a).
- (vi) Large isolated water-ice-rich features having lifetimes of more than 1.5 yr (Oklay et al. 2016a).
- (vii) Exposure of water ice via cliff collapse observed on Aswan (Pajola et al. 2017).

During the observations from August 2014 until the end of the *Rosetta* mission (2016 September), numerous features enriched in water ice disappeared and/or appeared. In this study, we concentrate on the water-ice-rich exposures that could be tracked for the whole duration of the mission via OSIRIS NAC, and report on their status at three epochs: arrival, before perihelion and after perihelion. Additional features that could be observed only during two of these epochs are not considered here, except for the Hapi region and an alcove on Seth. Our main targets are large clustered features (CFs), large IFs and the vicinities of RFs. All of these (Fig. 1) were first detected on the arrival at the comet on 2014-08-03 (Fig. 1a). However, due to the low spatial resolution of these first observations, we chose 2014-09-05 (Fig. 1b; Table 1) as starting epoch for CF1–3, IF1–2 and RF. Additionally to these areas, the Hapi region and an alcove in the Seth region are included in our study due to long-term stability of the observed water ice.

Using OSIRIS NAC images, we investigate the multispectral and morphological changes of these features along with their vicin-



(a)



(b)

**Figure 1.** Locations of the investigated features displayed on RGB colour composites. Images taken at 989.3.1 and 701.2 nm are used in the R and G channels, while 360.0 or 480.7 nm images are used for the B channel according to the availability (see Table 1 for available data). (a) Water-ice features at the arrival to the comet (#1 in Table 1). (b) Water-ice features on 2014-09-05. Image mosaic is generated by using the image sets #3–#5, #13, #14 in Table 1.

ity's at the three main epochs of 2014 August and September (arrival), 2015 March–May (pre-perihelion) and 2016 January (post-perihelion). One large feature is additionally investigated at two additional epochs (2016 May and July). We quantify the temporal variation of the multispectral signatures of those features. Associated activity events (jets and outburst) are also investigated together with morphological changes. In water-ice-rich features observed on large debris fields, imaging at different epochs allows us to estimate the material loss from the surface. By calculating the energy input on to those features, we derive the sublimation rate and estimate the thickness of the existing water ice. By performing spectral modelling, we estimate the water ice abundances in the selected boulders within clusters and in the large isolated patches observed on 2014 September.

**Table 1.** Multispectral NAC images used for the temporal evolution analysis of the features enriched in water ice.

Image ID	Acquisition date	UT	Central wavelength (nm)	$r$ (au)	Resolution (m px <sup>-1</sup> )	Phase angle (°)
#1	2014-08-03	04:22:59	480.7, 535.7, 649.2, <b>701.2</b> , 743.7, 805.3, 882.1, 989.3	3.61	6.38	33.06
#2	2014-08-22	01:41:55	360.0, 480.7, 535.7, <b>649.2</b> , 701.2, 743.7, 805.3, 882.1, 989.3	3.51	1.21	34.84
#3	2014-09-05	05:31:25	360.0, 535.7, 649.2, <b>701.2</b> , 743.7, 882.1, 989.3	3.43	0.76	57.37
#4	2014-09-05	06:36:14	360.0, 535.7, 649.2, <b>701.2</b> , 743.7, 882.1, 989.3	3.43	0.76	57.76
#5	2014-09-05	06:46:25	360.0, 535.7, 649.2, <b>701.2</b> , 743.7, 882.1, 989.3	3.43	0.76	57.85
#6	2015-03-10	21:32:15	<b>480.7</b> , 649.2, 882.1	2.13	1.6	55
#7	2016-01-24	01:06:56	480.7, <b>649.2</b> , 882.1	2.04	1.37	61.08
#8	2016-04-28	07:19:43	360.0, 480.7, 535.7, <b>649.2</b> , 701.2, 743.7, 805.3, 882.1, 931.9, 989.3	2.89	0.3	92.8
#9	2015-05-16	12:54:10	269.3, 360.0, 480.7, 535.7, 649.2, 701.2, 743.7, 805.3, <b>882.1</b> , 931.9, 989.3	1.62	2.32	62.09
#10	2016-05-02	12:14:10	360.0, 480.7, 535.7, 649.2, 701.2, <b>743.7</b> , 805.3, 882.1, 931.9, 989.3	2.92	0.31	62.09
#11	2016-07-30	01:37:15	480.7, <b>649.2</b> , 882.1	3.48	0.17	103
#12	2014-09-05	05:37:33	360.0, 535.7, 649.2, <b>701.2</b> , 743.7, 882.1, 989.3	3.43	0.76	57.34
#13	2014-09-05	06:32:00	360.0, 535.7, 649.2, <b>701.2</b> , 743.7, 882.1, 989.3	3.43	0.76	57.85
#14	2014-09-05	02:56:57	360.0, 535.7, 649.2, <b>701.2</b> , 743.7, 882.1, 989.3	3.43	0.76	90

Notes. Acquisition time (UT) is given for the reference image. Reference images are indicated in bold. Image IDs are used as a reference in all images displayed in this work.

## 2 DATA AND ANALYSIS METHODS

The OSIRIS NAC is equipped with 11 filters in the wavelength range of 250–1000 nm (see Keller et al. 2007, for further details). Various filter combinations were used during the observational sequences to fulfil various scientific goals. All images used in this study have been radiometrically calibrated and corrected for optical distortion and are expressed radiance factors ( $I/F$ ):

$$I/F = \frac{\pi r^2 I_m}{F_{\odot}}, \quad (1)$$

where  $I_m$  is the measured intensity in radiance units ( $\text{W m}^{-2} \text{nm}^{-1} \text{sr}^{-1}$ , at the central wavelengths of each filter),  $F_{\odot}$  is solar flux at 1 au measured at the central wavelength for each filter and  $r$  is the heliocentric distance of the comet in au.

### 2.1 OSIRIS NAC multispectral images

All subsequently taken OSIRIS NAC multispectral images given in Table 1 are co-aligned to eliminate colour artefacts occurred due to the combined effects of comet rotation and spacecraft's orbital motion during imaging. Both pixel shifts and rotations are considered during the sub-pixel accurate registration of the images. In order to reduce the effects of different illumination conditions, all images are photometrically corrected using Lommel-Seeliger disc law (Hapke 1993). This photometric correction is adopted, since it is shown by Fornasier et al. (2015) to be adequate for the resolved nucleus images of comet 67P. Both image alignment and photometric correction are achieved by using the Integrated Software for Imagers and Spectrometers (USGS ISIS3,<sup>1</sup> Anderson et al. 2004). The Lommel-Seeliger disc function is defined as

$$D(i, e) = \frac{2 \cos(i)}{\cos(i) + \cos(e)}, \quad (2)$$

where  $D$  is the disc function,  $i$  and  $e$  are the incidence and emission angles respectively. Disc-corrected images are then obtained by dividing the  $I/F$  images by the disc function (equation 2). In order to

reduce artefacts arising for extreme geometries, in the photometrically corrected images, the regions with angles larger than  $80^\circ$  were excluded.

The photometric angles were calculated from the global cg-dlr\_spg-shap7-v1.0 shape model (Preusker et al. 2017). As well as its precursor, i.e. the cg-dlr\_spg-shap4s-v1.0 shape model (Preusker et al. 2015), it has been derived from stereo-photogrammetric analysis (SPG) and consists of more than 40 million facets with a typical point spacing of 1–2 m. The photometric angles are derived by numerically placing and orienting the shape model at the J2000 location of the comet at the observing time of the reference images (bold in Table 1). The location is provided by ephemeris data from ESA flight dynamics (Planetary Science Archive SPICE repository<sup>2</sup>). The comet attitude is derived from the comet body fixed CHEOPS coordinate frame (NAIF ID: 67P/C-G\_CK). Using a geometric model of the OSIRIS cameras, the intersection point between the view ray and the shape model is calculated for each pixel in the image. The surface normal of the intersection point is calculated using a linear interpolation scheme between the shape vertex-point normal's of the shape facet being intersected. Each step for the production of photometrically corrected and co-aligned multispectral data from subsequently taken OSIRIS NAC images are described in Oklay et al. (2016b, appendix A).

The coordinates and approximate sizes of each selected water-ice-rich feature are given in Table 2 with references to earlier water-ice studies and the associated activity event. All these areas are marked on a comet map (Fig. 2) to present their distribution on a global scale. In order to have a direct comparison of the images taken at various spatial resolutions at different times, and viewing geometries, we projected spectral products on to the 3D shape model using the SHAPEVIEWER software,<sup>3</sup> and displayed them in a common frame.

### 2.2 Spectral methods

Spectral slopes are used to detect the spectral changes of the investigated water-ice patches over time. Due to observational limitations

<sup>2</sup> ftp://psa.esac.esa.int/pub/mirror/INTERNATIONAL-ROSETTA-MISSION/SPICE/RO-RL-E-M-A-C-SPICE-6-V1.0/

<sup>3</sup> http://www.comet-toolbox.com/shapeViewer.html

<sup>1</sup> http://isis.astrogeology.usgs.gov/index.html

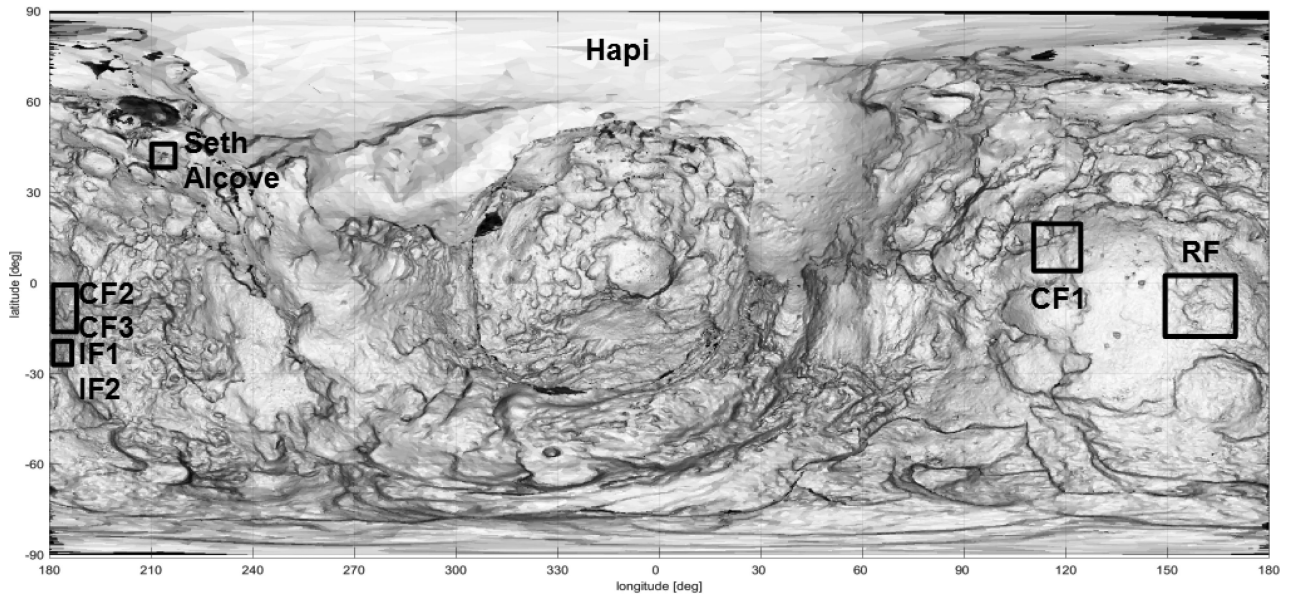
**Table 2.** Coordinates of the features given in Fig. 2. Longitudes are in 0–360°, latitudes are in ± 90 domains.

ID	Lon., Lat. (°)	Type	Approximate area <sup>a</sup> (m <sup>2</sup> )	Early prediction of water ice via multispectral analysis	water-ice reference	Associated activity features
CF1	117, 13 N	clustered features	8373.8	–	Filacchione et al. (2016b, BAP1)	–
CF2	180, 2 S	clustered features	14652.8	Oklay et al. (2016b)	Filacchione et al. (2016b, BAP2)	Jets <sup>b,c</sup>
CF3	182, 8 S	clustered features	4652.2	Oklay et al. (2016b)	This study	Jets <sup>b</sup>
RF	170, 10 S	roundish features	–	Oklay et al. (2016a)	Filacchione et al. (2016a)	Outburst <sup>d</sup>
IF1	183, 21 S	isolated features	126.5	Oklay et al. (2016b)	Barucci et al. (2016, spot5)	–
IF2	183, 22 S	isolated features	74.5	Oklay et al. (2016b)	This study	–
SA	213, 41 N	Seth alcove	3900	Oklay et al. (2016b)	–	Jets <sup>b</sup>

<sup>a</sup>On 2014 images given Table 1.

<sup>b</sup>Vincent et al. (2016b).

<sup>c</sup>Oklay et al. (2016b).

<sup>d</sup>Knollenberg et al. (2016).

**Figure 2.** Distribution of long-lived water-ice-rich areas (black rectangles), introduced in Table 2, on comet 67P. This map is a cylindrical projection of cg-dlr-spg-shap7-v1.0 (Preusker et al. 2017). The top of the small lobe is at about 0°, 0° (in the middle), while the bottom of the big lobe is centred about –20°, 130°.

during imaging, multispectral observations of comet 67P were performed in various number of filters in different combinations (see Table 1 for the data sets). The spectral slope definition used in this study is

$$\text{Spectral slope (per cent per 100 nm)} = \frac{(R_2 - R_1) \times 10^4}{(\lambda_2 - \lambda_1) \times R_1}, \quad (3)$$

where  $R$  represents the radiance factors in the given filters, with their central wavelengths located at wavelengths  $\lambda$ .

In the investigation of CF1–3, IF1–2 and RF, the only two common filters (see Table 1) centred at 649.2 and 882.1 nm are used for the spectral slope calculation, while investigation of Hapi and of the Seth alcove (SA) were performed using the filters centred at 535.7 and 882.1 nm to be consistent with previous studies.

The spectral slope increase of  $0.104 \times 10^{-4} \text{ nm}^{-1} \text{ deg}^{-1}$  by phase angle (phase reddening) was measured by Fornasier et al. (2015) using summer 2014 images of the resolved nucleus. The evolution of the nucleus phase reddening by heliocentric distance is summarized in Fornasier et al. (2016, fig. S3). In order to be not affected by the phase reddening, we investigated our main features (Fig. 1) in images taken at similar phase angles where the reddening is neg-

ligible. We used images #3–#7 given in Table 1 to investigate the features CF1–3, RF and IF1–2. Here, we note that the phase angle difference between these images are 55°–61°, small enough for the phase reddening to be negligible (Fornasier et al. 2015). Unfortunately, the selection of Hapi and SA images at similar phase angles were not possible due to lack of suited observations. Therefore, the phase reddening correction is applied to those images. The comparison of Hapi region at two epochs is done by using images #2 and #9 (phase angles 35°–62°), which are corrected for phase reddening using the method by Fornasier et al. (2016). The images of the SA used in this study are #2, #8 (phase angles 35°–92°), which are also corrected by phase reddening.

Water ice has no specific spectral features in the OSIRIS wavelength range that are diagnostic to derive physical properties. However, water ice and typical non-volatile cometary material can be individually spectrally modelled under the assumption of areal mixing. In this approach, the individual materials within the mixture are considered non-interacting, and the combined signal is the sum of fractional area times the spectrum of each component (Clark 1999):

$$R = p \times R_{\text{ice}} + (1 - p) \times R_{\text{MC}}, \quad (4)$$

where  $R$  is the reflectance of the water-ice feature,  $R_{\text{ice}}$  is the reflectance of water ice calculated using optical constants of water ice from Warren & Brandt (2008),  $R_{\text{MC}}$  is the mean cometary terrain in the vicinity of the water-ice feature and  $p$  is the fractional area of the water-ice feature.

The same method was applied to various water-ice exposures observed on comet 67P to study the water-ice content (Fornasier et al. 2016, 2017). Therefore, we adopt the same methodology to investigate the water content of the features IF1–2, and couple of boulders within clusters CF1–3 (see Table 2 for feature IDs and coordinates), that were observed on 2014-09-05 images. The selected boulders are typically 3–6 times brighter than their vicinity and all have flat spectra with spectral slopes lower than 6 per cent per 100 nm. We calculated the mean reflectance spectra of the selected features by using  $3 \times 3$  px boxes. Normal albedo of the features is then calculated using photometrically corrected images and Hapke modelling (Hapke 2002) with the parameters derived in Fornasier et al. (2015, table 4). The description of the method is given in the supplementary materials of Fornasier et al. (2016) in details. Here, we note that we adopted a water-ice grain size of 30  $\mu\text{m}$ , which is a typical size for ice grains on cometary nuclei (Sunshine et al. 2006; Filacchione et al. 2016b). The same assumption is also used in other studies (Fornasier et al. 2016, 2017). This assumption is needed since we cannot put constraints on the grain sizes from OSIRIS images.

### 2.3 Thermal analysis

In order to assess the survivability of water ice over long time-scales, the sublimation process for the water-ice-rich areas is investigated by using the thermophysical model A described in Keller et al. (2015). In this model, the contribution of the surface thermal conductivity to the thermal balance is considered negligible, and the surface is assumed to reach instantaneous thermal equilibrium under the effects of solar input, re-irradiation and latent heat of sublimation. Because topography and illumination geometry control the energy input, we made use of the shape model SHAP4S (Preusker et al. 2015) to extract a local digital terrain model (DTM) of the area containing the patches (see Table 2). The resulting DTM, which has a resolution in the order of 2 m, enables us to accurately model insolation, self-shadowing and self-heating in this region.

For a given macroscopic albedo, the amount of solar energy absorbed by a cometary surface depends on the (unresolved) scale at which ice and opaques are mixed. Since we cannot infer the type of mixing from imaging, we considered the following two end cases, which correspond to maximum and minimum sublimation rate from the bright patches, respectively:

(i) Water ice and dust are intimately mixed down to submillimetre scales in the form of dirty ice. Dust particles and ice are assumed to be in thermal equilibrium and therefore have the same temperature. The surface-integrated albedo controls the sublimation of the ice patch. The Bond albedo of the ice patch is set to  $A_b = 0.05$ , or five times larger than the one of average 67P terrain to match the albedo of the observed water-ice-rich features (Fornasier et al. 2016).

(ii) Dust and (pure) water ice are each organized in homogeneous units larger than 1 mm but still smaller than the resolution limit (areal mixing). Ice and dust particles are segregated, and assumed not to interact thermally with each other, and to reach two different equilibrium temperatures. The sublimation rate is computed individually for the two components, with the sublimation rate of pure ice being the driver for the observed permanence time of the bright

**Table 3.** VIRTIS cubes used for the detection of water ice.

Cube ID	Acquisition time (UT)	$r$ (au)	Resolution (m px <sup>-1</sup> )	Phase angle (°)
00377182711	2014-12-14T12:59:43	2.77	5	92.0
00377184571	2014-12-14T13:30:43	2.77	5	92.7

*Notes.* Acquisition time (UT) is given for the starting time of the observations. Durations of each observation are 13 and 12 min, respectively.  $d$  is comet spacecraft distance. All data are in reflectance (radiance factor).

patches. The Bond albedo of pure-ice regions in the patch has been set to  $A_b = 0.7$ , as in the case of clean snow (Delsemme 1985).

In order to estimate erosion, water production rates were integrated along the orbit with constant steps in mean anomaly of approximately  $3^\circ$  for the period 2014 September 5 – 2016 February 2 for the features CF1–3 and IF1–2 for which water ice was confirmed in the IR wavelengths (Barucci et al. 2016; Filacchione et al. 2016b). The resulting erosion is reported in Fig. 10 expressed in terms of a pure solid-ice equivalent thickness. This quantity can be readily transformed into erosion of porous dirty ice once dust/ice ratio and porosity are assumed.

### 2.4 Size distribution of water-ice-rich features

The size frequency distribution for boulders enriched in water ice was discussed in Pommerol et al. (2015) and Oklay et al. (2016a). In the latter, boulder statistics was combined with multispectral information (blue-edged neighbouring cliffs) to investigate the formation mechanisms of large clusters enriched in water ice. In order to detect possible boulder disappearance or size changes of the water ice features, we re-analysed the same features (CF1–3 and IF1–2) presented in Oklay et al. (2016a, figs. 8 and 9) using the images taken on 2015-03-10 (#6 in Table 1).

Out of four different clusters of boulders (including CF1–3), where we identified a fitting power-law index (Oklay et al. 2016a, fig. 8), the only bright boulder group that provided a good statistics of remnants is CF2. Here, we applied the same methodology of Oklay et al. (2016a) to derive the maximum sizes of the bright remnant boulders; that is, we draw a circle around those shapes and by knowing the scale per pixel we derived their dimensions in metre. We then binned with 1 m size the boulder cluster (as in Oklay et al. 2016a) and obtained the cumulative number of boulder per each size. For the clusters CF1 and CF3, where it is not possible to derive a power-law index due to small statistics, we only measured the sizes of the boulders that are enriched in water ice. For large IFs enriched in water ice (IF1, IF2) the sizes on 2015-03-10 are measured.

### 2.5 IR spectral data

Water ice was detected in the infra-red (IR) wavelengths within CF1, CF2, IF1 and RF (see Table 2 for references). For CF3 and IF2, we investigated the existence of water-ice bands in IR wavelengths by extracting spectra from the data sets given in Table 3 within  $3 \times 3$  px boxes centred at the coordinates given in Table 2. The IR spectral data were acquired by the Visible and InfraRed Thermal Imaging Spectrometer-Mapper (VIRTIS-M-IR; Coradini et al. 2007) onboard *Rosetta*. The VIRTIS data given in Table 3 are available publicly in ESA's PSA archive.<sup>4</sup> The 2.0  $\mu\text{m}$  water-ice

<sup>4</sup> <https://www.cosmos.esa.int/web/psa/rosetta>

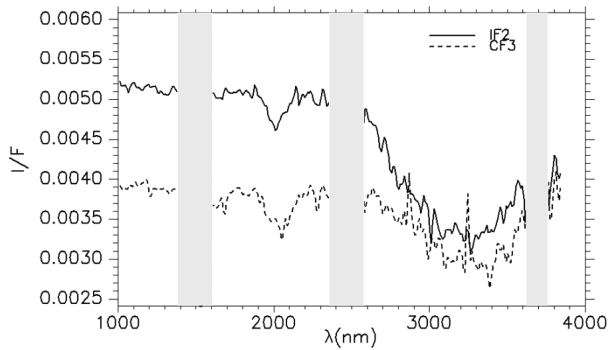


**Figure 3.** Water-ice detection on features CF3 and IF2 using IR spectroscopy. Greyed out regions are the instrumental order sorting filter junction locations. See Clark et al. (2013, fig. 1.2) for the laboratory spectra of water ice.

band in is clearly evident (Fig. 3) in the spectra of the observed features in CF3 and IF2 together with the 3.0  $\mu\text{m}$  water-ice band that is contaminated by the bands of existing organic material. A detailed information on the spectral properties of the water ice can be found in Clark et al. (2013) and Mastrapa, Grundy & Gudipati (2013). Further investigation of these features in the IR wavelengths is beyond the scope of our work.

The detection of water ice in SA requires more detailed investigation of the IR spectra, and is an ongoing work. However, it is possible to use wavelengths in the visible range to detect water-ice patches. Since the first multispectral observations of cometary nuclei, the bright blue nature of the water-ice-rich features in the visible wavelengths was used as a diagnostic indicator of ice presence. Moreover, for comet 67P several water-ice-rich areas (including CF1, CF2, CF3 and IF1 from Table 2) were investigated in both visible and IR wavelengths, which led to the identification of a correlation between visible slopes and IR slopes (Raponi et al. 2016; Weller 2016).

### 3 RESULTS

The water-ice-rich features given in Table 2 are investigated using the images in Table 1 in smaller regions including the feature and its vicinity. We first present a general view on the features using colour composite images and spectral slopes, and then present our results per feature in the following subsections.

#### 3.1 General view on the features

Water-ice-rich features are blue in the RGB composites generated by using the images taken at near-infra-red (NIR), visible and near-ultraviolet (NUV) wavelengths, and have lower spectral slopes than their vicinity. For all features given in Table 2, we presented their temporal evolution at various epochs using Fig. 4 (CF1–3, IF1–2), Fig. 5 (RF), Fig. 6 (SA) and Fig. 7 (Hapi region). We see the blue nature of the features in 2014 images and the variation over time in the top panels, while corresponding spectral slopes (see equation 3) are given at the respective bottom panels for the epochs given in the figure captions. The spectral slopes are between 5 and 11 per cent per 100 nm in 2014 images. Even though most of the features decrease in size over time, their spectral slopes remain in the same range. Not every feature decays over time: RF became bluer and then redder again, SA became bluer, and while the Hapi region seemed to remain the same. The details of the variation per region will be discussed in the following subsections.

All features given in Table 2 were observable at the arrival to the comet on 2014 August. Fig. 1(a) shows the blue nature of the extended Imhotep features in the early images taken with filters centred at different wavelengths. This suggest that these large water-ice patches were formed during the previous orbit of the comet.

The morphology of long-lived water-ice-rich patches is consistent across the surface. The ‘blue’ area in our colour composite typically corresponds to the talus of a local collapsed topography such as a cliff, pit, alcove or overhangs. Such structures are ubiquitous on 67P (Thomas et al. 2015a), with many being associated with dust jets and outbursts (Vincent et al. 2016a,b). A statistical description of 67P’s cliffs and erosion processes is available in Vincent et al. (2017). Our current understanding is that any vertical feature on the comet will eventually collapse under the stresses of gravity, activity and thermomechanical forces. Upon collapse, fresh material is exposed on the cliff wall (Pajola et al. 2017), but also in the debris fields that form the talus (Lucchetti et al. 2017). Additionally, the rough nature of the talus may also create permanently shadowed areas that can retain ice for a long time, or allow it to deposit for a while until it becomes exposed to insolation again. This also may be the case for the few bright spots that are not associated with a talus but still in a distinctly rough terrain, such as the RFs at the edge of the smooth Imhotep plain.

We analysed features individually and present our results per feature in the following subsections.

#### 3.2 Analysis of CF1

This cluster is located by a 200 m wide cliff (Fig. 4a) and consists of numerous boulders enriched in water ice in 2014 (the left-hand panel of Fig. 8). Overall, it is about two times brighter than its vicinity, while individual boulders are up to six times brighter at the first epoch. As seen in the top left-hand panel of Fig. 4(a), this cluster has a bright-blue talus extending up to 200 m away from its neighbouring cliff in 2014 observations, while it extends only up to 125 m away from its neighbouring cliff in 2015 (the middle top panel of Fig. 4a). The blue edge of the neighbouring cliff is still blue during the 2015 March observations. All water ice in the talus field is sublimated over 1.5 yr (2016-01-24).

The spectral slopes of the talus enriched in water ice is 8 per cent per 100 nm in 2014 and increases to 11 per cent per 100 nm in 2015. However, in 2015 there are still numerous boulders with spectral slopes as low as the ones observed on 2014 September (Fig. 4b). The increase in spectral slope is due to the reduction in number or water-ice-rich boulders within the talus over time. The spectral slopes where this cluster was located is the same as its vicinity in 2016 observations indicating that all exposed water ice was sublimated away around the perihelion passage.

We see a significant reduction in the number of water-ice-rich boulders we can detect in this talus field (Fig. 8) from 2014 to 2015. The number of bright boulders is 11, all with much lower sizes than the ones observed in 2014 (Fig. 8). The two biggest remnants on 2015-03-10 have a diameter of 6.9 and 3.9 m, respectively (see the right-hand panel of Fig. 8).

It is difficult to detect the lifetime of this cluster due to the limited high spatial resolution observations performed by OSIRIS NAC. This cluster still exists in 2015 April observations and its size reduces significantly until 2015-05-02. It is tentatively detectable in at this last epoch. This detection would make CF1 observable via OSIRIS NAC for about 10 months. However, we cannot

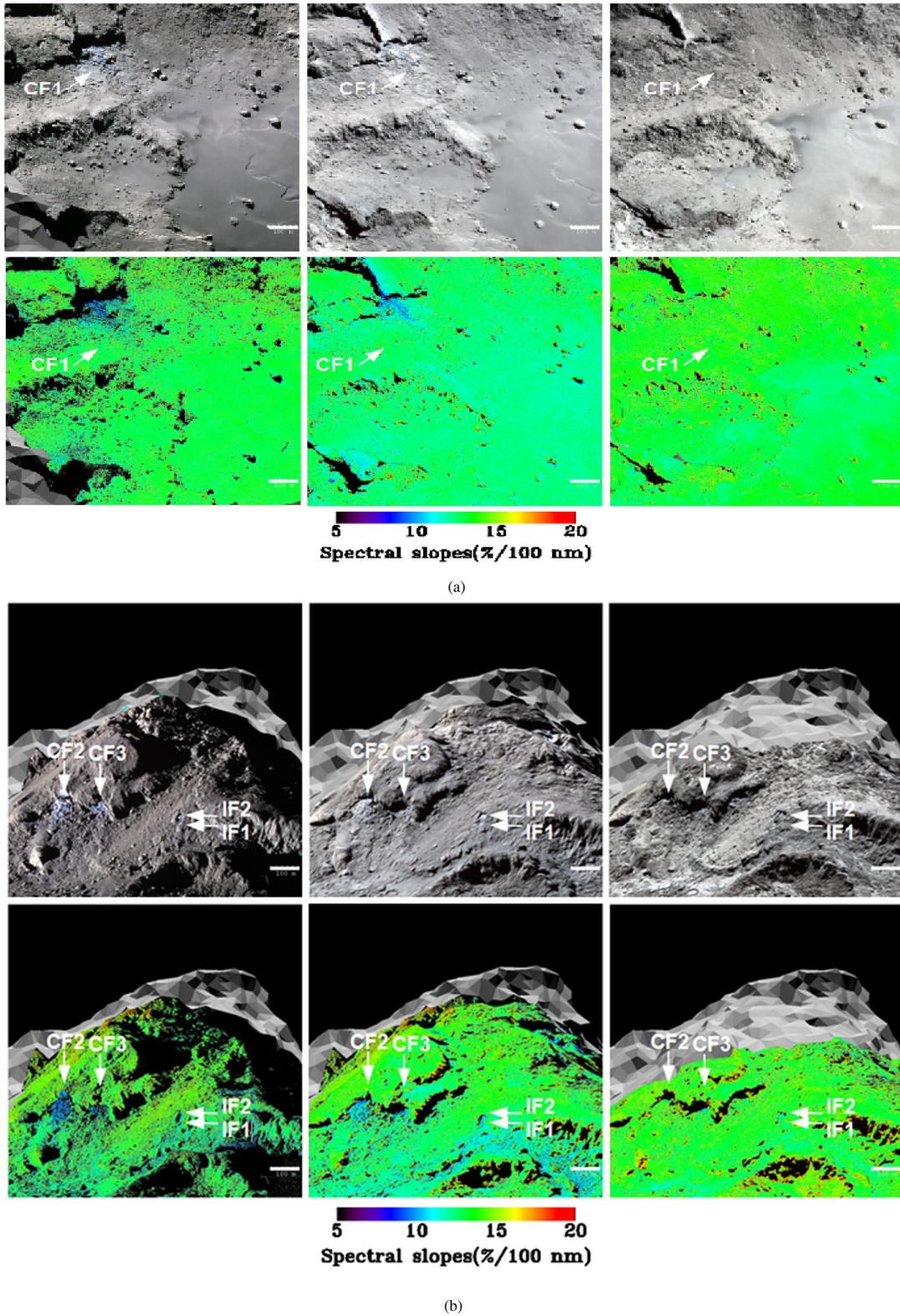


**Figure 4.** CF1, CF2, IF1 and IF2 at three epochs of 2014, 2015 and 2016 from left-hand to right-hand panels. White scale-bar on the right corners indicate 100 m. All images are projected on to 3D shape and displayed in a common frame to see the features in the same orientation. Images taken at 882.1 and 649.2 nm are used in the R and G channels, while 360.0 or 480.7 nm images are used for the B channel according to the availability (see Table 1 for available data). (a) CF1: RGB colour composites (top panels) and spectral slopes (bottom panels). Images are #5–#7 (Table 1) from left to right. (b) CF2, CF3, IF1 and IF2: RGB colour composites (top panels) and spectral slopes (bottom panels). Images are #4, #6, #7 (Table 1) from left to right.

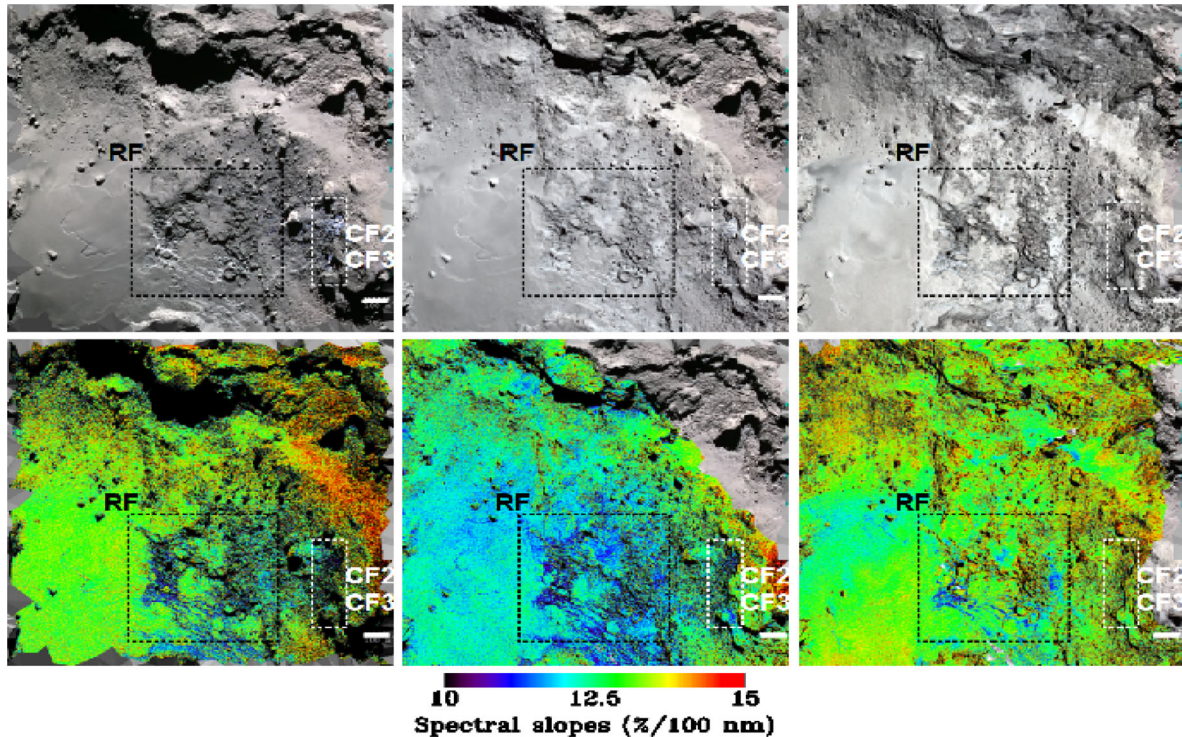


**Figure 5.** RF: RGB colour composites (top panels) and spectral slopes (bottom panels) of RF in 2014, 2015 and 2016 images from left to right respectively. Images are #12, #5, #7 (Table 1) from left to right. White scale-bar on the right corners indicate 100 m. All images are projected on to 3D shape and displayed in a common frame to see the features in the same orientation. Images taken at 882.1 and 649.2 nm are used in the R and G channels, while 360.0 or 480.7 nm images are used for the B channel according to the availability (see Table 1 for available data).

exactly determine when all the water ice was sublimated in this feature.

Using the image set #5 (Table 1), we selected three blue boulders enriched in water ice (the left-hand panel of Fig. 9a) within this cluster and modelled their spectra with their surroundings (maroon selection in the left-hand panel of Fig. 9a). Our spectral modelling (Fig. 9a) estimates 24.5 per cent, 10 per cent and 6.5 per cent water ice in the boulders shown in red, green and magenta, respectively. The boulder selected in red is the survivor given in Fig. 8 with a diameter of 6.9 m on 2015 March.

For CF1, using the erosion of pure ice equivalent calculated via thermal modelling, we estimate water-ice thickness of 0.7 cm in the case of areal and 13 cm in the case of intimate mixtures (the top panels of Fig. 10).

There were no activity found associated with this cluster. However, this might be due to observing conditions unfavourable for the activity detection.

### 3.3 Analysis of CF2

This cluster is located by a 125 m wide cliff and about two times brighter than its vicinity in 2014. As seen in the top left-hand panel of Fig. 4(b), its blue talus extends up to 150 m away from the neighbouring cliff in 2014 and decreases to 100 m away in 2015 (the middle top panel of Fig. 4b) showing the effects of sublimation in the field. The blue edge of the neighbouring cliff seen in 2014 is sublimated away between these two epochs. The blue talus is still detectable until May 2015 with very few blue boulders. However, due to the low spatial resolutions of the following observations, we cannot characterize the sublimation of the blue talus more precisely.

Only very little amount of water ice seems to be preserved in a couple of boulders very close to the cliff on 2016.

The spectral slopes of the talus enriched in water ice is 8 per cent per 100 nm in 2014 and increases to 11 per cent per 100 nm in 2015. However, there are still numerous boulders with spectral slopes as low as the ones detected in 2014 (Fig. 4b). The increase in the spectral slopes is due to the reduction in number or water-ice-rich boulders within the talus over time.

CF2 was the only cluster where we could re-investigate the size-frequency distribution of the water-ice-rich boulders on 2015 March images. As seen in Fig. 11, the cumulative number of boulders  $>4$  m reduced from 55 to 25, while the power-law index extracted by fitting the cumulative number from 4 to 10 m flattened from  $-3.5$  to  $-2.4$ . This shows a clear reduction on the number of small boulders.

Using the image set #4 (Table 1), we selected boulders enriched in water ice (left-hand panel of Fig. 9b) within this cluster and modelled their spectra with their surrounding (yellow selection in the left-hand panel of Fig. 9b). Our spectral modelling results (Fig. 9b) suggest 18 per cent, 20 per cent and 6.5 per cent water ice in the boulders shown in red, green and blue, respectively. The boulders in red and blue are the ones still contributing to the boulder statistics on 2015 March (Fig. 11).

For CF2, using the erosion of pure ice equivalent calculated via thermal modelling, we estimate water-ice thickness of 0.45 cm in the case of areal and 11 cm in the case of intimate mixtures (the bottom panels of Fig. 10).

Several times there were jets observed associated with this cluster. See Oklay et al. (2016b) and Vincent et al. (2016b) for visualizations.

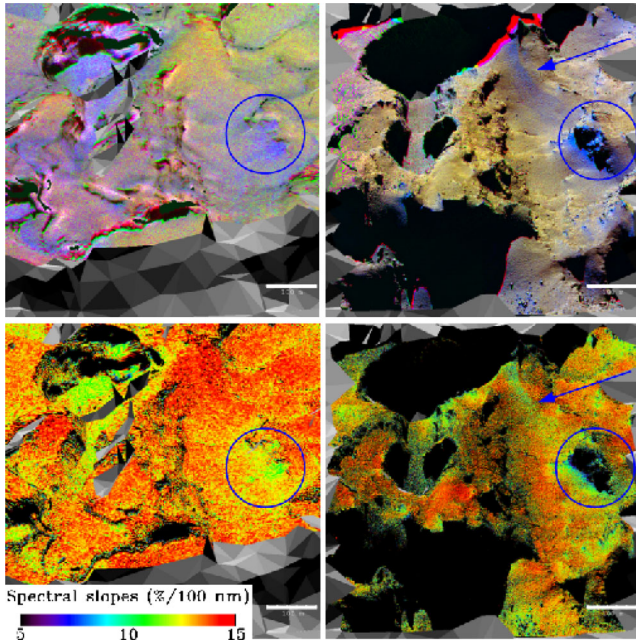


**Figure 6.** Water-ice-rich cliff on Seth. Top panel shows the blue SAs on 2014-08-22 (#2 in Table 1) and on 2016-04-28 (#8 in Table 1) images. All images are projected on to 3D shape to emphasize the topography. Decorrelation stretch (Gillespie, Kahle & Walker 1986) is applied to the top panel images to emphasize the minor colour differences. Corresponding spectral slopes are at the bottom panels. Spectral slopes given at the right-hand bottom panel (#8 in Table 1) are corrected for the phase reddening using Fornasier et al. (2016) for a comparison to 2014 observations. Blue circles indicate the location of the SA, while blue arrow indicates an exposure of potentially water-ice-rich material. White scale-bars show 100 m. Both images are projected on to 3D shape and displayed in a common frame to see the features in the same orientation.

### 3.4 Analysis of CF3

Compared to CF1 and CF2, this is a small cluster located by a 100 m wide cliff, and about twice brighter than its vicinity in 2014. As seen in the left-hand panel of Fig. 4(b), the blue talus of this cluster extends up to 75 m away from the neighbouring cliff in 2014, while it reduced to 50 m in 2015 observations (the middle top panel of Fig. 4b). The lifetime measurement of CF3 is the same as CF1 and CF2. Similar to CF2, a small amount of water ice seem to be preserved by the cliff on 2016-01-24 (the right-hand panels of Fig. 4b).

The spectral slopes of the talus enriched in water ice is 8 per cent per 100 nm in 2014 and increases to 11 per cent per 100 nm in 2015 (the bottom panels of Fig. 4b). However, we can still detect couple of boulders with spectral slopes as low as the ones detected in 2014 (the middle bottom panel of Fig. 4b). The increase in the spectral slopes is due to the reduction in number or water-ice-rich boulders within the talus over time.

Almost all boulders enriched in water ice disappeared on 2015 March except the two boulders in which the largest one surviving with similar size (see Fig. 12).

Using the image set #4 (Table 1), we selected two water-ice-rich boulders (the left-hand panel of Fig. 9c) within this cluster and modelled their spectra with their surrounding (blue selection in the left-hand panel of Fig. 9c). Our spectral modelling results (Fig. 9c) suggest 15.5 per cent and 19 per cent water ice for the boulders se-

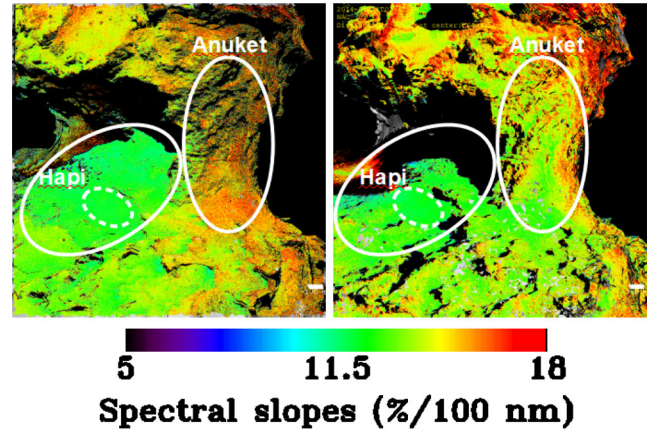


**Figure 7.** Spectral slopes of Hapi region. Left-hand panel is the spectral slopes of Hapi region on 2014-08-22 (#2 in Table 1), while the right-hand panel is the similar view on 2015-05-16 (#9 in Table 1). 2016 observation is corrected for phase reddening using Fornasier et al. (2016). Both images are projected on to 3D shape and displayed in a common frame to see the features in the same orientation. White ellipses indicate the regions, while dashed ellipses indicate the common part of the Hapi in both images where there are no shadows. The areas marked with dashed ellipses were used for the comparison of spectral slopes at two epochs.

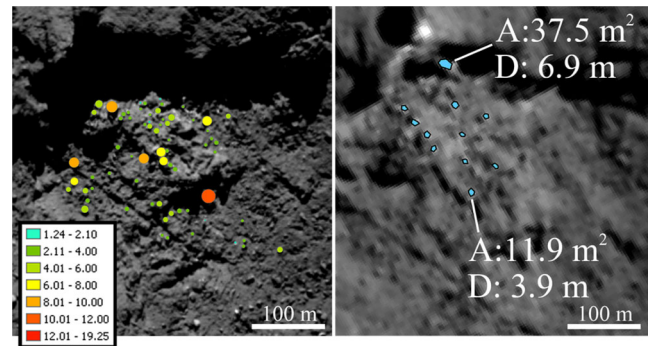


**Figure 8.** Water-ice-rich boulders of CF1. Left-hand panel shows the statistics on 2014-09-05 (#5 in Table 1), while right-hand panel shows the same area on 2015-03-10 (#6 in Table 1) images. Areas are given with A, while diameters are with D.

lected in red and green, respectively. The boulder selected in green is one of the survivors seen in Fig. 12.

For CF3, using the erosion of pure ice equivalent calculated via thermal modelling, we estimate water-ice thickness of 0.9 cm in the case of areal, and 9 cm water ice in the case of intimate mixtures (the bottom panels of Fig. 10).

There were jets observed in this feature. See Vincent et al. (2016b) for details.

### 3.5 Analysis of IF1

The area of IF1 is 126.5 m<sup>2</sup> (see Oklay et al. 2016a, fig. 9) in the 2014 September observations (image #4, Table 1) and is about two times brighter than its vicinity. This feature had a dramatic reduction in size within 8 months and is 28.5 m<sup>2</sup> (Fig. 13) on 2015 March. It is tentatively detectable on 2015 April in low spatial resolutions.

The spectral slopes of IF1 is  $\sim 5$  per cent per 100 nm on 2014 September and increases to 10 per cent per 100 nm on 2015 March (Fig. 4b). Since all available water ice is sublimated away

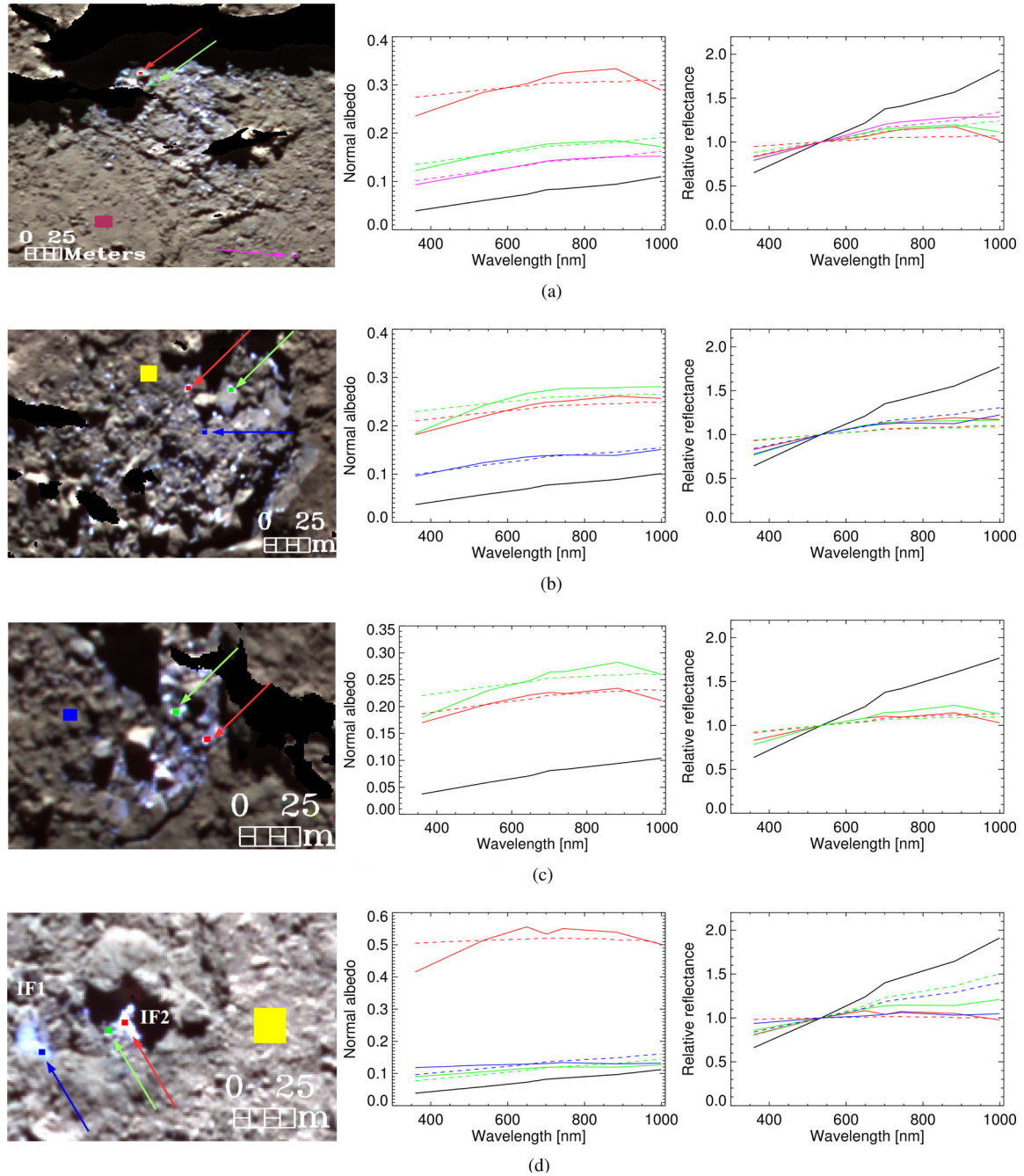


**Figure 9.** Spectral modelling of selected water-ice-rich features observed on 2014-09-05. Left-hand panels are CF1, CF2, CF3, IF1 and IF2 in RGB colour composites with selected rois overlaid in colours from top to bottom panels, respectively. Images taken at 989.3, 701.2 and 360.0 nm are used in the RGB channels, respectively. Image set #6 is used at the top panel, while image set #5 is used in the rest of the panels. The largest selection boxes represent the vicinity of the features. Corresponding albedo and the relative reflectance (normalized at 535.7 nm) are in the middle and right-hand panels, respectively. In the spectral profiles, solid lines represent the average spectra of the rois with the corresponding modelled spectra in dashed lines in the same colours. Black lines in the spectral plots (middle and right-hand panels) represent the vicinity of the selected features. (a) CF1: red 24.5 per cent water ice + 75.5 per cent MC, green 10 per cent water ice + 90 per cent MC, magenta 6.5 per cent water ice + 93.5 per cent MC. (b) CF2: red 18 per cent water ice + 82 per cent MC, green 20 per cent water ice + 80 per cent MC, blue 6.5 per cent water ice + 93.5 per cent MC. (c) CF3: red 15.5 per cent water ice + 84.5 per cent MC, green 19 per cent water ice + 81 per cent MC. (d) IF1 and IF2: red 48 per cent water ice + 52 per cent MC, green 4 per cent water ice + 96 per cent MC, blue 6 per cent water ice + 94 per cent MC.

possibly before 2015 May, the spectral slopes of the area where this feature was located are the same as its vicinity on 2016 January observations.

Using image #4 (Table 1), we modelled its spectra in the brightest part (blue in the left-hand panel of Fig. 9d) of this feature with its

vicinity (yellow in the left-hand panel of Fig. 9d). Our spectral modelling results (Fig. 9d) suggests 6 per cent water-ice abundance in this feature.

Using the erosion of pure ice equivalent calculated via thermal modelling, we estimate water-ice thickness of 0.9 cm in the case of

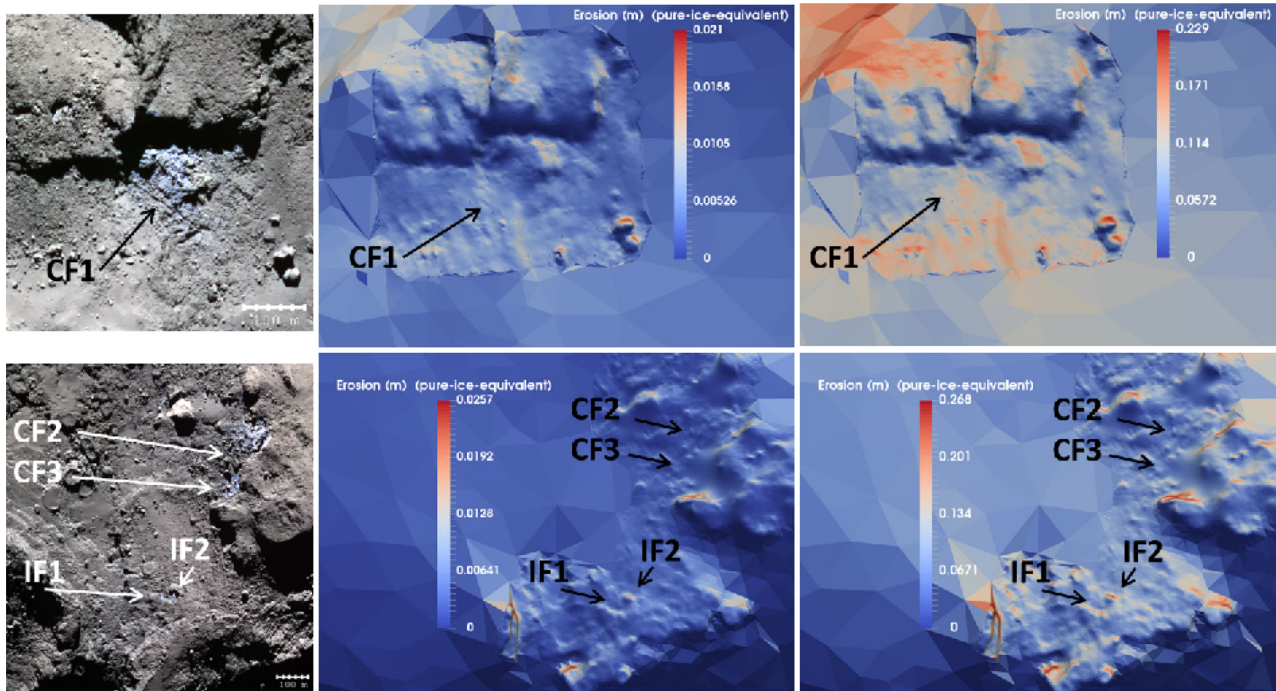


**Figure 10.** Erosion integrated between the first two epochs of 2014 September and 2015 March. CF1 (top panels), CF2–3 (mid panels), IF1–2 (bottom panels) in geographic and intimate mixing of water ice and dust from middle to right-hand panels, respectively. Left-hand panels show investigated features using the colour composites generated by assigning images taken at 989.3, 701.2 and 360.0 nm to the RGB channels, respectively. Image set #6 is used at the top panel, while image set #5 is used at the bottom panel. The orientation of the features are the same as Fig. 9.

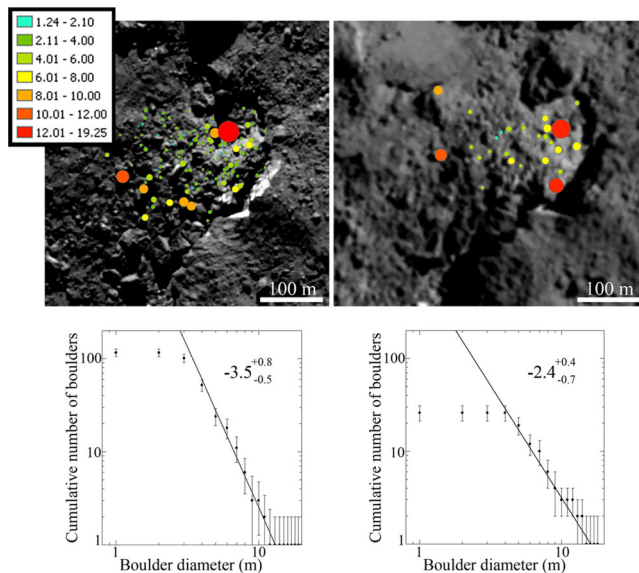


**Figure 11.** Water-ice-rich boulders of CF2. Left-hand panels show the detected boulders with their sizes (top panel) and corresponding statistics (bottom panel) on 2014-09-05 (#4 in Table 1) while right-hand panels are the same area on 2015-03-10 (#6 in Table 1) images.

areal and 15 cm in the case of intimate mixtures (the bottom panels of Fig. 10).

No activity is observed associated with this feature. However, this might be an observational bias. As seen in 2014 images (the top left-hand panel of Fig. 14a), this feature does not appear with sharp boundaries in RGB colour composites but is a fuzzy structure. This could be a sign of ongoing sublimation.

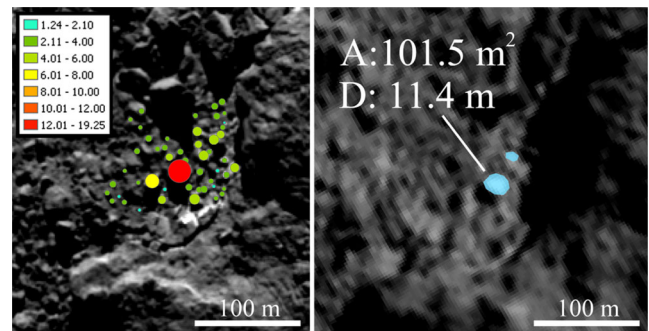


**Figure 12.** Water-ice-rich boulders of CF3. Left-hand panels show the boulder statistics on 2014-09-05 (#4 in Table 1), while right-hand panel is the same area on 2015-03-10 (#6 in Table 1) images. Areas are given with A, while diameters are with D.

### 3.6 Analysis of IF2

IF2 is a large isolated patch located in a cavity. There are several large boulders located around this feature (see Fig. 14a). Its size is about 75 m<sup>2</sup> (see Oklay et al. 2016a, Fig. 9) in 2014 September observations (image #4, Table 1) and is about eight times brighter than its vicinity. Its size decreases down to 53 m<sup>2</sup> in 2015 March observations (Fig. 13), and its brightness is three times less. While its brightness decreases over time, its spectrum becomes slightly redder (the top panel of Fig. 14b). We can still detect this feature in the observations of 2015 May observations with low spatial resolutions (2.4 m px<sup>-1</sup>). Unfortunately, IF2 was observed only at spatial resolutions (3–12 m px<sup>-1</sup>) from 2015 June to 2015 December, which makes its size or spectral variations difficult to estimate. However, whenever this cavity was illuminated, we could detect some bright features.

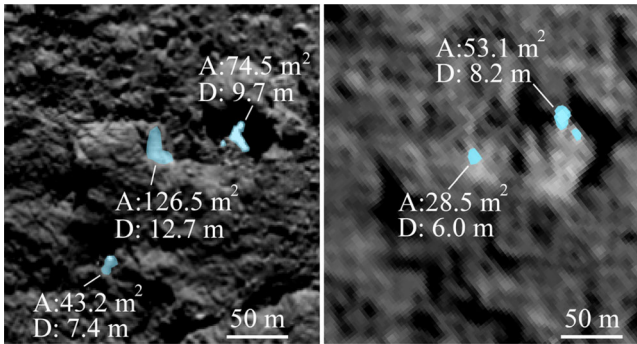


**Figure 13.** Sizes of IF1 (mid feature) and IF2 (right feature) at two epochs. The left-hand panel shows the sizes on 2014-09-05 (#4 in Table 1) observations, while the right-hand panel shows the measurements on 2015-03-10 (#6 in Table 1) images. Areas are given with A, while diameters are with D.

Using the image #4 (Table 1), we modelled its spectra (red in the left-hand panel of Fig. 9d) along with its vicinity (yellow in the left-hand panel of Fig. 9d). Our spectral modelling results (Fig. 9d) suggests 48 per cent water-ice abundance. We could also observe a boulder (green in the left-hand panel of Fig. 9d) by this feature, and our modelling suggests 6 per cent water ice for this small exposure.

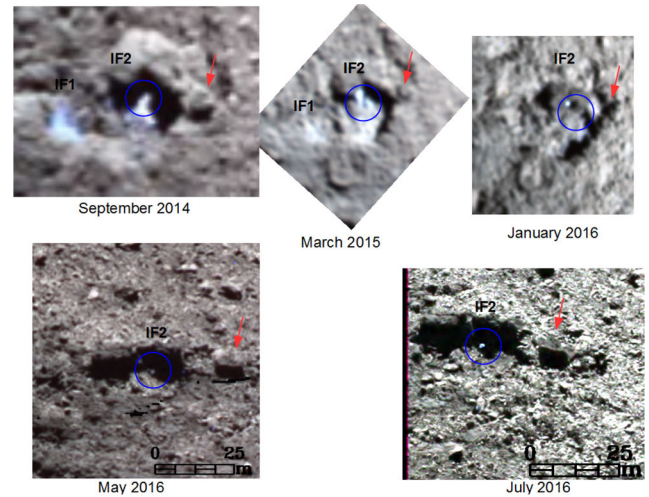
The surprising thing about IF2 is that we could still detect it on 2016 January images (the top right-hand panel of Fig. 14a) once we could again observe the same area in high spatial resolutions. In January 2016, we see this structure as one very bright blue round feature and two irregular shaped ones. We can track the blue boulder until February 13, but there is no image set from the same region until 2016 May 02 due to low spatial resolution and/or not ideal viewing geometry. On 2016 May 02, we observed this region again (the bottom left-hand panel of Fig. 14a) and detected a slightly bluer spectrum than its surrounding (see the bottom panel of Fig. 14b). However, this blue feature is not well illuminated at this epoch. Therefore, its spectrum is not investigated further. On 2016 July, we found that the same boulder observed on 2016 May can be resolved in 30 pixels ( $0.17 \text{ m px}^{-1}$ ), and it became three times brighter than its vicinity and bluer. Once we combine all these data sets, and make a comparison using relative reflectance, we see that this boulder became redder (still bluer than its surrounding), and then bluer again. This might be explained by the sublimation-regeneration (new layer of water-ice exposure or local enhancement or removal of dust) cycle.

It is difficult to estimate water-ice thickness of this feature. If we assume 2016 mid-February as the date of its disappearance, our water-ice thickness estimates would be 38 cm in the case of areal and 186 cm in the case of intimate mixtures (the bottom panels of Fig. 10). However, one boulder seems to have survived longer than this period as described in the previous paragraph.

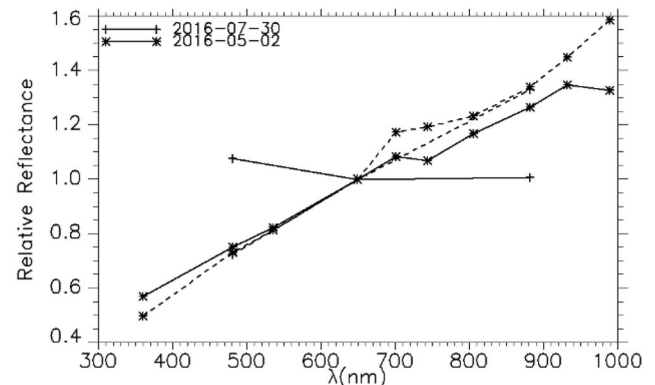
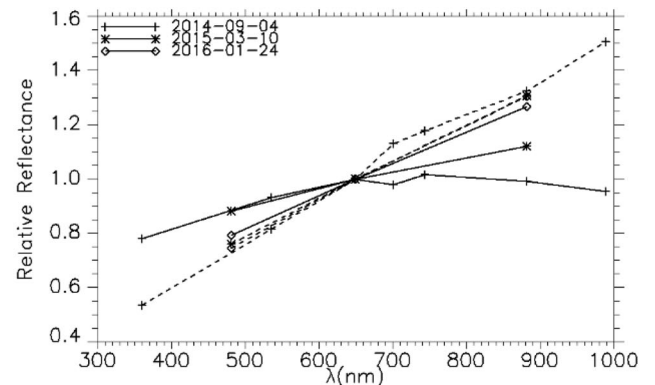
No activity associated with this feature was observed.

### 3.7 Analysis of RF

In 2014 September (image #4, Table 1), the vicinity of the RFs appear green in the RGB colour composites (the left-hand panel of Fig. 5). Opposite to the other investigated features described earlier, it is getting bluer around the RFs from 2014 September to 2015 March (the top panels of Fig. 5). Once the mean spectral slope values around the RFs are investigated over time, we see that the overall changes of the slopes are 1 per cent per 100 nm. The mean spectral slopes of same area we measured in 2014 is 11 per cent per



(a)



(b)

**Figure 14.** IF2 at 5 epochs. The top panel is the RGB colour composites, while the plots in the bottom panel shows the corresponding spectra. Images taken at 882.1 and 649.2 nm are used in the R and G channels, while 360.0 or 480.7 nm images are used for the B channel according to the availability (see Table 1 for available data). (a) RGB colour composites of IF2 at 5 epochs. Image sets #5–#7, #10 and #11 (Table 1) are used from first epoch to the last one, respectively. (b) Multispectra of IF2 at 5 epochs. The top panel shows the reflectance of IF2 at the first 3 epoch with its vicinity (dashed lines), while the bottom panel shows the same at the two epochs of 2016. The spectra are normalized at 649.2 nm.

100 nm, while it is 10 per cent per 100 nm in 2015, and 11 per cent per 100 nm in 2016. The morphological changes in the region between 2015 and 2016 exposed sub-surface water ice.

The source of the outburst studied by Knollenberg et al. (2016) is in this region.

### 3.8 Analysis of SA

One of the alcoves (blue circles in Fig. 6) in the Seth region is as blue as the Hapi region and the active pits in 2014 observations (image set #2, Table 1). This alcove was always detectable due to its blue colour and lower spectral slopes than its surrounding. Surprisingly, it became bluer and observed as a very striking feature in 2016-04-28 observations (the top right-hand panel in Fig. 6). The spectral slopes of this alcove is 11 per cent per 100 nm similar to the active Seth pits, Hapi region and water-ice-rich features in 2014 observations. The spectral slopes decrease to 9 per cent per 100 nm in 2016 observations. The cliff edges, pit rims and rough areas have lower spectral slopes than their vicinity in both epochs indicating regions enriched in water ice. Additionally, a potential water-ice-rich exposure, from the edge of the largest pit extending as a band-like flow towards the alcove, has notable low spectral slopes. This is potentially a water-ice exposure due to erosion on the cliff rim. There were jet detections in this region (Vincent et al. 2016b).

### 3.9 Analysis of Hapi

Hapi is a region  $\sim 16$  per cent brighter than the mean surface and with lower spectral slopes (Fornasier et al. 2015). Spectral properties of the Hapi region are similar to large water-ice-rich clusters (Oklay et al. 2016b). The mean spectral slope of the common regions observed at the two epochs is 12 per cent per 100 nm and there is no spectral change within the selected area between the period of 2014-08-22 and 2015-05-16 (Fig. 7) even though this region was the most active at the arrival to the comet and there were jets observed during the entire mission. This issue is discussed in Keller et al. (2017) in details.

## 4 DISCUSSIONS

Long-term high spatial resolution multispectral imaging of comet 67P allowed us for the first time to follow features surviving up to 1.5 yr. Our multispectral analysis shows the existence of water-ice-rich features on the comets' surface that are not potentially much mixed with the dust. These are large features surviving more than a year. The fact that they can survive for such long time-scales supports the idea of the mixing of water ice with relatively low amount of dust. However, local topography plays a big role on the survival of the most longevous water-ice-rich feature, since it is located in a cavity and protected by a boulder. A potential additional mechanism that prevents water ice from sublimating is that its temperature is kept low through super-volatile sublimation. Of course such a sublimation-driven cooling would require high concentration of hyper-volatiles which is not very likely to survive the high insolation in the Imhotep region. We would like to note that we cannot exclude the possibility that these features disappeared around comet's perihelion passage and were later reformed. This is due to the difficulty in tracking these features between 2015 June and December. In this period, the spatial resolutions were varying between 3 and 12 mpx<sup>-1</sup>. Each time the locations of these features were illuminated, they were much brighter than their vicinity. But a confident analysis on the size and spectral variation requires

higher spatial resolutions in order to detect them in at least  $3 \times 3$  px areas. However, the fact that we see those water-ice-rich exposures again at the same locations indicates that there was enough water ice in the subsurface to regenerate them even if these features had completely disappeared. Regeneration can here mean several things. One process is the covering and exhumation of a larger reservoir of subsurface ice via dust accretion and dust clearing. A very thin layer of dust is already sufficient to mask the icy appearance. Another possible process is the actual growth of the ice layer via recondensation of water on to the ice rich layer. The second process is, however, unlikely. Given the fact that the regions receive significant insolation with the diurnal cycle, it is difficult to imagine a new growth of volatile water ice under these conditions. Another problem is that the source reservoir of water ice is insufficient. The sublimating water molecules must come from the subsurface ice reservoir. However, water can only sublimate from inside the diurnal thermal skin depth which is only of the order of a centimetre given the very low thermal inertia of the cometary surface material. We see many examples of potential surface recondensation of water ice (De Sanctis et al. 2015; Fornasier et al. 2016). These surface frosts are, however, only very thin layers that re-sublimate in a few minutes after the surface gets illuminated by the Sun.

Using OSIRIS multispectral imaging, the global spectral slope changes of the comet over time was earlier presented by Fornasier et al. (2016). We see spectral slopes variations on the extended Imhotep region at the epochs we investigated. The region has 1–2 per cent per 100 nm lower spectral slopes during the perihelion passage in 2015 as compared to the 2014 observations. The spectral slope values are high again comparable to 2014 in the 2016 observations. We do not detect any spectral slope variation on the parts of the Hapi and Seth regions that could be observed on 2014 August and 2015 May images (Table 1, #2 and #16, respectively).

There are several large (talus extending up to 200 m away from its neighbouring cliff, which is about 100 m wide) clusters consisting of numerous 1–20 m sized boulders enriched in water ice. Such debris fields survive at least 10 months from 2014 August until 2015 May. The blue taluses reduce significantly until 2015 March and disappear towards the perihelion (2015 August 13). Dust jets associated with these clusters were observed by Vincent et al. (2016b) and Oklay et al. (2016b). The detection of dust activity shows the availability of more dust within these clusters than the large IFs.

From 2014-09-05 to 2015-03-10, we detected significant size reduction in IF1 and IF2 (IF2 almost disappeared within this period) and in numerous boulders enriched in water ice within CF1–3. Only large boulders on CF2–3 seem to have similar sizes at these two epochs. It was only possible to study the size frequency distribution in CF2 due to the low number of ice-enriched boulders in the 2015-03-10 images. The observed flattening of the power-law index within 7 months is due to large boulders generally surviving on the surface (partially shrinking in size), while smaller boulders drastically reduced in number due to sublimation. Such changes in the power-law indices due to sublimation were earlier predicted by Pajola et al. (2016).

Filacchione et al. (2016b) modelled the IR spectra of CF1 and CF2 to estimate the water-ice abundance and the grain sizes. Simultaneous simulation of intimate (3.4 per cent water ice, 56  $\mu\text{m}$ ) and areal (1–2 per cent water ice, 1960  $\mu\text{m}$ ) mixtures provided the best modelling results. Our spectral modelling estimates similar abundances on some boulders within the same clusters. However, we additionally observe boulders containing up to 25 per cent water ice. The IR spectra modelling of IF1 performed by Barucci et al. (2016) achieved the best fits by non-simultaneous modelling of

**Table 4.** Water-ice estimations and comparison of OSIRIS and VIRTIS results.

Feature ID	VIS modelling (2014-09-05)	IR modelling (+10, +40, +100 d after) <sup>a</sup>
CF1	6–25 per cent	<6 per cent (Filacchione et al. 2016b)
CF2	6–20 per cent	<6 per cent (Filacchione et al. 2016b)
CF3	15–10 per cent	–
IF1	6 per cent	<2 per cent (Barucci et al. 2016)
IF2	48 per cent	–

<sup>a</sup>See Section 4 for the observation dates of different features.

intimate (2 per cent, 800 $\mu$ m) and areal (1.7 per cent, 400  $\mu$ m) mixtures. Our spectral modelling estimates a slightly higher water-ice abundance (see Table 4 for summary). These differences are due to the combined effects of different spatial scales (the high spatial resolutions that the OSIRIS-NAC achieved), observing and illumination geometry, and epoch of observation. Note that OSIRIS multispectral images have a pixel scale of 0.76 m px<sup>-1</sup>, while VIRTIS IR spectra had 2.2 m px<sup>-1</sup> ( $\sim$ 3 times lower than our study) for CF1, 7.7 m px<sup>-1</sup> ( $\sim$ 10 times lower than our study) for CF2 and 5.5 m px<sup>-1</sup> ( $\sim$ 7 times lower than our study) for IF1. The lower VIRTIS spatial resolution results in contamination from the non-icy vicinity within pixels. Moreover, IR observations of CF1 were performed  $\sim$ 40 d, CF2  $\sim$  10 d and IF1  $\sim$  100 d after the multispectral imaging that is used in our study to assess temporal variability. Our analysis shows that during these time intervals all water-ice-rich patches considered here reduced in size. A direct comparison of this situation is possible for IF1. Its diameter was 12.7 m in 2014-09-05, while Barucci et al. (2016) reported 6.5 m in 2014-11-22. From our analysis, we estimate about 42 m<sup>2</sup> size reduction within this time frame. Local topography also plays a big role on the investigation of IF2 since it is located in a cavity. These observations, performed by two different instruments, were taken under different observing geometries resulting in different illumination conditions.

Temporal evolution of CF1 and CF2 was investigated using the visible and IR slopes from the VIRTIS data (Raponi et al. 2016). Even though these clusters were detectable in the high spatial resolution OSIRIS NAC images (1.6 m px<sup>-1</sup>) taken on 2015 April, Raponi et al. (2016) reported their disappearance at the end of 2015 February and beginning of 2015 March in the observations with spatial scales of 20 m px<sup>-1</sup>. This missed detection was probably not only due to the low spatial resolutions of VIRTIS but also due to the unfavourable observing conditions (viewing geometry, local topography effects).

The spectral slopes were used since the first multispectral observations of cometary nuclei via space-borne observations as a diagnostic tool for water-ice deposits. The correlation of visible and IR slopes of CF1–3 and IF1–2 are presented by Weller (2016). Using VIRTIS data of CF1 and CF2, Raponi et al. (2016) presented the insensitivity of the visible slopes to the grain size but the sensitivity to the abundance and the type of mixing. The decrease in the reflectance of IF2 and some boulders within clusters towards the IR wavelengths indicate the existence of water-ice absorption band at 1.05  $\mu$ m.

Vicinity of the RFs were already predicted to be active by Oklay et al. (2016b) using the 2014-09-05 observations due to their green colour and low spectral slopes. This was proven by the observations investigated by Knollenberg et al. (2016). Oklay et al. (2016a) showed that the region becomes bluer with time and concluded that this is possible due to the removal of dust and exposure of subsurface

water ice from beneath. This idea is also supported by the photometric studies of Hasselmann et al. (2017). In our current study, we detected some morphological changes in this region leading to the exposure of water ice from beneath. Filacchione et al. (2016a) detected water ice in the region hosting RFs by monitoring the 2  $\mu$ m band between 2014 August and 2014 December. Further investigation of this area in the IR wavelengths will help us to understand better this potential water-ice reservoir.

In the most longevous feature IF2, we see size reduction and brightness change over time. This large feature observed on 2014-09-05 seems to be split into two smaller features before the following 2015-03-10 observations. The larger one was still observable in 2016-01-24 observations. Additionally, a new water-ice exposure was observable at that epoch. This suggests the survival of the water-ice reservoir. The reduction in brightness between 2014-09-05 and 2015-03-10 is about 66 per cent, while the reduction in brightness between 2015-03-10 and 2016-01-24 is about 30 per cent. This shows that the feature changed the most within the first 7 months period and it was decreasing in size and in brightness more slowly during the next 10 months. However, this brightness reduction might be due to the lower spatial resolutions, i.e. contamination from the non-icy vicinity, of the second and third epoch observations. During the same period, normalized reflectance values show that the spectra become slightly redder over time. The changes of the spectra are difficult to interpret due to the limited number of filters (Fig. 14b) and the unknown contamination from the non-icy surface. By comparing the spectra given in Fig. 14(b) with Fig. 9(d), we expect a decrease in the reflectance with IR wavelengths. A bright blue boulder is detected in the 2016-05-02 observations at the same location as one of the three features observed on 2016 January images. This boulder is visible until the last observation of this area in 2016-07-30. As of the last detection, it is about three times brighter than its vicinity. The changes in time can be explained by the sublimation and regeneration cycle. However, in order to come to a firm conclusion, we need consider the spatial resolution effects and the phase difference of the images ( $\sim$ 60° in the first three epochs and  $\sim$ 90° in the last two epochs).

For all investigated features except IF2, ice thickness estimations are about between 0.5 and 15 cm. The lower values are obtained in the areal mixture case where water ice and dust are thermally not interacting therefore less energy is available for sublimation. The higher values correspond to the intimate mixing case where both components are in thermal equilibrium; therefore, more energy is available for sublimation. It is difficult to estimate the water-ice thickness for IF2 due to its unknown lifetime. Since we can trace it until 2016 February observations, we estimate between 40 and 180 cm of water ice. There are no observations allowing for us to track this feature until 2016 May when we see a bright blue boulder at the same location until the last observation of this region in 2016 July. Therefore, we consider our water-ice thickness estimates as lower limits.

Seth is a region with large pits ( $\sim$ 200 m in diameter) where dust jets were observed. This region hosts many alcoves, which have bluer spectral properties than their surrounding (Oklay et al. 2016b). Inversion of dust jets detected those alcoves as the activity sources for the jets (Vincent et al. 2016b). The alcove investigated in this study is the one next to the active pits and was observed since August 2014. It was blue in the first images, with lower spectral slopes than its surrounding. However, this alcove became significantly bluer during the 2016-04-28 observations. The fact that this feature was active suggests the possible continuous exposure of water ice from beneath.

It has been proposed by Keller et al. (2017) and Thomas et al. (2015b) that the back fall of ice rich material transported from the active regions of the comet on the Southern hemisphere is the source of the early onset of jet activity originating from the Hapi and Seth regions. Ice-rich back fall would also explain the bluer spectral slope detected when the Seth region came out of the Northern winter season in 2016.

Hapi was the most active region at the arrival to the comet. Due to its high albedo and low spectral slopes, it was predicted to contain water ice by Fornasier et al. (2015). From the IR spectroscopy, diurnal cycle of re-condensed water ice was detected by De Sanctis et al. (2015). Therefore, it is interesting to study this region at different epochs. This, however, was a challenge since Hapi was not observable from mid 2015 observations on. Between 2014-08-22 and 2015-05-16, we do not detect any significant change in the spectral slopes of this region, even though it was active for a long time and lost lots of dust and volatiles. This might be explained by two possibilities. One is that fresh, ice-rich airfall material originating from the Southern hemisphere (Thomas et al. 2015b) feeds the upper layers so that the spectral properties of the region remains the same (Keller et al. 2017). The second possibility is that the top layers of this region are composed of small grains of well-mixed dust and water ice so that losing the dust with the activity and losing the volatiles via sublimation reveals the similar layers from beneath. This is also supported by similar observations of bright patches in Seth's circular niches (Lucchetti et al. 2017).

The long-term high spatial resolution multispectral observations presented in our study shows that longevous features enriched in water ice are not distributed on the entire comet surface but reside primarily in extended Imhotep. It is remarkable because this equatorial region is illuminated at each rotation, regardless of the perihelion distance, and therefore should have been one of the most depleted in volatiles. The fact that water-ice-rich material was detected in such area and survived unambiguously for several months can be due to several factors, all of them challenging the current understanding of comet formation and evolution. Indeed, it is mostly agreed that cometary nuclei are rather homogeneous in structure and composition. However, the presence of these patches enriched in water ice indicates that large reservoirs of rather pure ice (or at least with a low dust/ice mixing ratio) must exist under the surface to replenish continuously the exposed areas. This hints at structural heterogeneity in the distribution of volatiles and refractory material, which could potentially reflect heterogeneity in the comet's primitive constituents as well. As an alternative, one may also consider these patches to be very shallow, thus removing the need for a reservoir. But this would then impose conditions on the dust to ice mixing within these areas for the features to be longevous.

At this point in the study, we do not have enough input to choose between these scenarios, but both imply that cometary nuclei are probably less homogeneous than previously thought, with variations in ice content appearing at various scales, from centimetre to decametre. This local heterogeneity is likely primordial, or regions with similar erosion rate and illumination conditions would also display the same features. Therefore, our work indicates that the primitive cometary environment, at the time of comet formation, may have been more diverse than current models predict.

## 5 CONCLUSIONS AND OUTLOOK

We investigated the temporal evolution of water-ice features detected at the arrival of *Rosetta* spacecraft to comet 67P using OSIRIS NAC multispectral images. We modelled visible spectra to estimate

water-ice abundance within the selected features. Using the results of our thermal analysis, we estimated the water-ice thickness within those patches for the two end-member cases. Our main findings are as follows:

- (i) We detected a potential water-ice deposit surviving for the entire *Rosetta* mission.
- (ii) All large clusters enriched in water-ice survive for at least 10 months on the surface of a comet 67P.
- (iii) All these large long-lived water-ice-rich patches were possibly formed during comet's previous orbit, since they were observable at the arrival and disappeared afterwards.
- (iv) Local topography seems to play a big role in the exposure of water-ice-rich features and their sustainability. Large clusters are formed via cliff collapse, which exposed sub-surface water ice to the surface. Large IFs are located in a cavity. They might have been exposed to the surface when this cavity was formed possibly by activity.
- (v) All long-lived large water-ice-rich features detected in 2014 observations are located in between  $\pm 30^\circ$  latitudes and  $115^\circ$ – $200^\circ$  longitudes.
- (vi) The long survivability of isolated water-ice-rich features on comet 67P suggests a larger abundance of water ice in those features than in large clusters.
- (vii) We found water ice patches up to 15 cm thick, surviving at least 10 months long.
- (viii) We estimate up to 48 per cent water-ice abundance in the most longevous isolated water-ice feature at the detection time in 2014 September at a heliocentric distance of 3.4 au in inbound orbit.

## ACKNOWLEDGEMENTS

OSIRIS was built by a consortium of the Max-Planck-Institut für Sonnensystemforschung, Göttingen, Germany; CISAS University of Padova, Italy; the Laboratoire d'Astrophysique de Marseille, France; the Institutode Astrofísica de Andalucía, CSIC, Granada, Spain; the Research and Scientific Support Department of the European Space Agency, Noordwijk, the Netherlands; the Instituto Nacionalde Técnica Aeroespacial, Madrid, Spain; the Universidad Politécnica de Madrid, Spain; the Department of Physics and Astronomy of Uppsala University, Sweden; and the Institut für Datentechnik und Kommunikationsnetze der Technischen Universität Braunschweig, Germany. The support of the national funding agencies of Germany (DLR), France (CNES), Italy (ASI), Spain (MEC), Sweden (SNSB) and the ESA Technical Directorate is gratefully acknowledged. We thank the Rosetta Science Ground Segment at ESAC, the Rosetta Mission Operations Centre at ESOC and the Rosetta Project at ESTEC for their outstanding work enabling the science return of the *Rosetta* mission.

This project has received partial funding from the European Union's Horizon 2020 research and innovation programme under grant agreement no. 686709.

This research has made use of NASA's Astrophysics Data System Bibliographic Services.

This research has made use of the USGS Integrated Software for Imagers and Spectrometers (ISIS). We gratefully acknowledge the developers of SPICE and NAIF/PDS resources.

This research made use of the software *SHAPEVIEWER*, available at [www.comet-toolbox.com](http://www.comet-toolbox.com).

We appreciate the efforts of an anonymous reviewer that led to several improvements in this work.

## REFERENCES

- Anderson J. A., Sides S. C., Soltesz D. L., Sucharski T. L., Becker K. J., 2004, in Mackwell S., Stansbery E., eds, Lunar and Planetary Inst. Technical Report, Vol. 35, Lunar and Planetary Science Conference. p. 2039
- Barucci M. A. et al., 2016, *A&A*, 595, A102
- Clark R. N., 1999, Chapter 1: Spectroscopy of Rocks and Minerals, and Principles of Spectroscopy. John Wiley and Sons, Inc., p. 3
- Clark R. N., Carlson R., Grundy W., Noll K., 2013, in Gudipati M. S., Castillo-Rogez J., eds, *Astrophysics and Space Science Library*, Vol. 356, The Science of Solar System Ices. Springer Science+Business Media, New York, p. 3
- Coradini A. et al., 2007, *Space Sci. Rev.*, 128, 529
- De Sanctis M. C. et al., 2015, *Nature*, 525, 500
- Delsemme A. H., 1985, in Klinger J., Benest D., Dollfus A., Smoluchowski R., eds, *NATO Advanced Science Institutes (ASI) Series C*, Vol. 156. D. Reidel Publ. Co., Dordrecht, p. 367
- Deshapriya J. D. P. et al., 2016, *MNRAS*, 462, S274
- El-Maarry M. R. et al., 2015, *A&A*, 583, A26
- El-Maarry M. R. et al., 2016, *A&A*, 593, A110
- Filacchione G. et al., 2016a, *Icarus*, 274, 334
- Filacchione G. et al., 2016b, *Nature*, 529, 368
- Fornasier S. et al., 2015, *A&A*, 583, A30
- Fornasier S. et al., 2016, *Science*, 354, 1566
- Fornasier S. et al., 2017, *MNRAS*, 469, S93
- Gillespie A. R., Kahle A. B., Walker R., 1986, *Remote Sens. Environ.*, 20, 209
- Groussin O. et al., 2015, *A&A*, 583, A36
- Hapke B., 1993, *Theory of Reflectance and Emittance Spectroscopy*, 1st edn. Cambridge Univ. Press, Cambridge
- Hapke B., 2002, *Icarus*, 157, 232
- Hasselmann P. et al., 2017
- Keller H. U. et al., 2007, *Space Sci. Rev.*, 128, 433
- Keller H. U. et al., 2015, *A&A*, 583, A34
- Keller H. U. et al., 2017, *MNRAS*, 469, S357
- Knollenberg J. et al., 2016, *A&A*, 596, A89
- Lucchetti A. et al., 2017, *MNRAS*, 469, S238
- Mastrapa R. M. E., Grundy W. M., Gudipati M. S., 2013, in Gudipati M. S., Castillo-Rogez J., eds, *Astrophysics and Space Science Library*, Vol. 356, The Science of Solar System Ices. Springer Science+Business Media, New York, p. 371
- Oklay N. et al., 2016a, *MNRAS*, 462, S394
- Oklay N. et al., 2016b, *A&A*, 586, 18
- Pajola M. E. A. et al., 2017, *Nat. Astron.*, 1, 92
- Pajola M. et al., 2016, *A&A*, 592, A69
- Pommerol A. et al., 2015, *A&A*, 583, A25
- Preusker F. et al., 2015, *A&A*, 583, A33
- Preusker F., Scholten F., the OSIRIS Team, 2017, in Muinonen K., Penttilä A., Granvik M., Virkki A., Fedorets G., Wilkman O., Kohout T., eds, *Asteroids, Comets, Meteors 2017*.
- Raponi A. et al., 2016, *MNRAS*, 462, S476
- Sunshine J. M. et al., 2006, *Science*, 311, 1453
- Thomas N. et al., 2015a, *Science*, 347, aaa0440
- Thomas N. et al., 2015b, *A&A*, 583, A17
- Vincent J.-B. et al., 2016a, *MNRAS*, 462, S184
- Vincent J.-B. et al., 2016b, *A&A*, 587, A14
- Vincent J.-B. et al., 2017, *MNRAS*, 469, S329
- Warren S. G., Brandt R. E., 2008, *J. Geophys. Res.*, 113, D14220
- Weller D., 2016, Master's thesis, Univ. Potsdam
- <sup>1</sup>German Aerospace Center (DLR), Institute of Planetary Research, Rutherfordstraße 2, D-12489 Berlin, Germany
- <sup>2</sup>NASA Ames Research Center, Moffett Field, CA 94035, USA
- <sup>3</sup>LESIA, Observatoire de Paris, PSL Research University, CNRS, Univ. Paris Diderot, Sorbonne Paris Cité, UPMC Univ. Paris 06, Sorbonne Universités, 5 Place J. Janssen, F-92195 Meudon Principal Cedex, France
- <sup>4</sup>Institute for Geophysics and Extraterrestrial Physics, TU Braunschweig, D-38106 Braunschweig, Germany
- <sup>5</sup>Max-Planck-Institut für Sonnensystemforschung, Justus-von-Liebig-Weg 3, D-37077 Göttingen, Germany
- <sup>6</sup>Dipartimento di Fisica e Astronomia 'Galileo Galilei', University of Padova, vic. Osservatorio 3, I-35122 Padova, Italy
- <sup>7</sup>Laboratoire d'Astrophysique de Marseille, UMR 7326 CNRS & Aix-Marseille Université, 38 rue Frédéric Joliot-Curie, F-13388 Marseille Cedex 13, France
- <sup>8</sup>Centro de Astrobiología (INTA-CSIC), European Space Agency (ESA), European Space Astronomy Centre (ESAC), PO Box 78, E-28691 Villanueva de la Canada, Madrid, Spain
- <sup>9</sup>International Space Science Institute, Hallerstrasse 6, CH-3012 Bern, Switzerland
- <sup>10</sup>Research and Scientific Support Department, European Space Agency, NL-2201 Noordwijk, the Netherlands
- <sup>11</sup>Department of Physics & Astronomy, Uppsala University, Box 516, SE-75120 Uppsala, Sweden
- <sup>12</sup>PAS Space Research Center, Bartycka 18A, PL-00716 Warszawa, Poland
- <sup>13</sup>Department for Astronomy, University of Maryland, College Park, MD 20742, USA
- <sup>14</sup>LATMOS, CNRS/UVSQ/IPSL, 11 Boulevard d'Alembert, F-78280 Guyancourt, France
- <sup>15</sup>Center of Studies and Activities for Space, CISAS, 'G. Colombo', University of Padova, via Venezia 15, I-35131 Padova, Italy
- <sup>16</sup>INAF Osservatorio Astronomico di Padova, Vicolo dell'Osservatorio 5, I-35122 Padova, Italy
- <sup>17</sup>CNR-IFN UOS Padova LUXOR, via Trasea 7, I-35131 Padova, Italy
- <sup>18</sup>NASA Jet Propulsion Laboratory, 4800 Oak Grove Drive, Pasadena, CA 91109, USA
- <sup>19</sup>Department of Industrial Engineering, University of Padova via Venezia 1, I-35131 Padova, Italy
- <sup>20</sup>University of Trento, via Sommarive, 9, I-38123 Trento, Italy
- <sup>21</sup>INAF – Osservatorio Astronomico di Trieste, via Tiepolo 11, I-34143 Trieste, Italy
- <sup>22</sup>Aix Marseille Université, CNRS, LAM (Laboratoire d'Astro-physique de Marseille) UMR 7326, F-13388 Marseille, France
- <sup>23</sup>Instituto de Astrofísica de Andalucía-CSIC, Glorieta de la Astronomía, E-18008 Granada, Spain
- <sup>24</sup>Institute for Space Science, National Central University, 32054 Chung-Li, Taiwan
- <sup>25</sup>ESA/ESAC, PO Box 78, E-28691 Villanueva de la Cañada, Spain
- <sup>26</sup>Department of Information Engineering, University of Padova, via Gradenigo 6/B, I-35131 Padova, Italy
- <sup>27</sup>Physikalisches Institut, Sidlerstrasse 5, University of Bern, CH-3012 Bern, Switzerland

This paper has been typeset from a  $\text{\TeX}/\text{\LaTeX}$  file prepared by the author.